

Supplementary Materials for
**Observation of resilient propagation and free-space skyrmions in
toroidal electromagnetic pulses**

Ren Wang *et al.*

*Corresponding author: Ren Wang (rwang@uestc.edu.cn) and Yijie Shen (yijie.shen@ntu.edu.sg)

1. Coaxial horn antenna for the generation of microwave Hellwarth-Nouchi toroidal pulses

The structural parameters of the broadband conical coaxial horn antenna used to generate microwave electromagnetic toroidal pulses are depicted in Fig. S1. The antenna comprises inner and outer conductors made of metal, with 3D-printed conical and flat-shaped dielectric supports at the bottom and top of the coaxial horn, respectively. The dielectric material possesses a dielectric constant of 1.3. To reduce the weight of the entire coaxial horn, the interior of the inner conductor is hollowed out. The antenna is fed from the bottom of the conical structure using a 2.92 mm coaxial connector with the rotationally symmetric TEM mode (radial polarization), where the inner and outer conductors of the connector are connected to the inner and outer conductors of the coaxial horn.

The measured reflection coefficient for this coaxial horn antenna is shown in Fig. S2, and it remains below -10 dB in the 1.3-10 GHz frequency range. This indicates that the designed coaxial horn's operating bandwidth can cover the spectral range below 10 GHz for generating electromagnetic toroidal pulses with parameters $q_1 = 0.01\text{m}$ and $q_2 = 50q_1$ (see Fig. 3). From Fig. S2, it is evident that the broadband conical coaxial horn antenna can operate in frequency bands exceeding 10 GHz. However, this study focuses on frequencies below 10 GHz due to the limitations of our spatial field measurement system, and therefore, the frequency bands above 10 GHz are not presented.

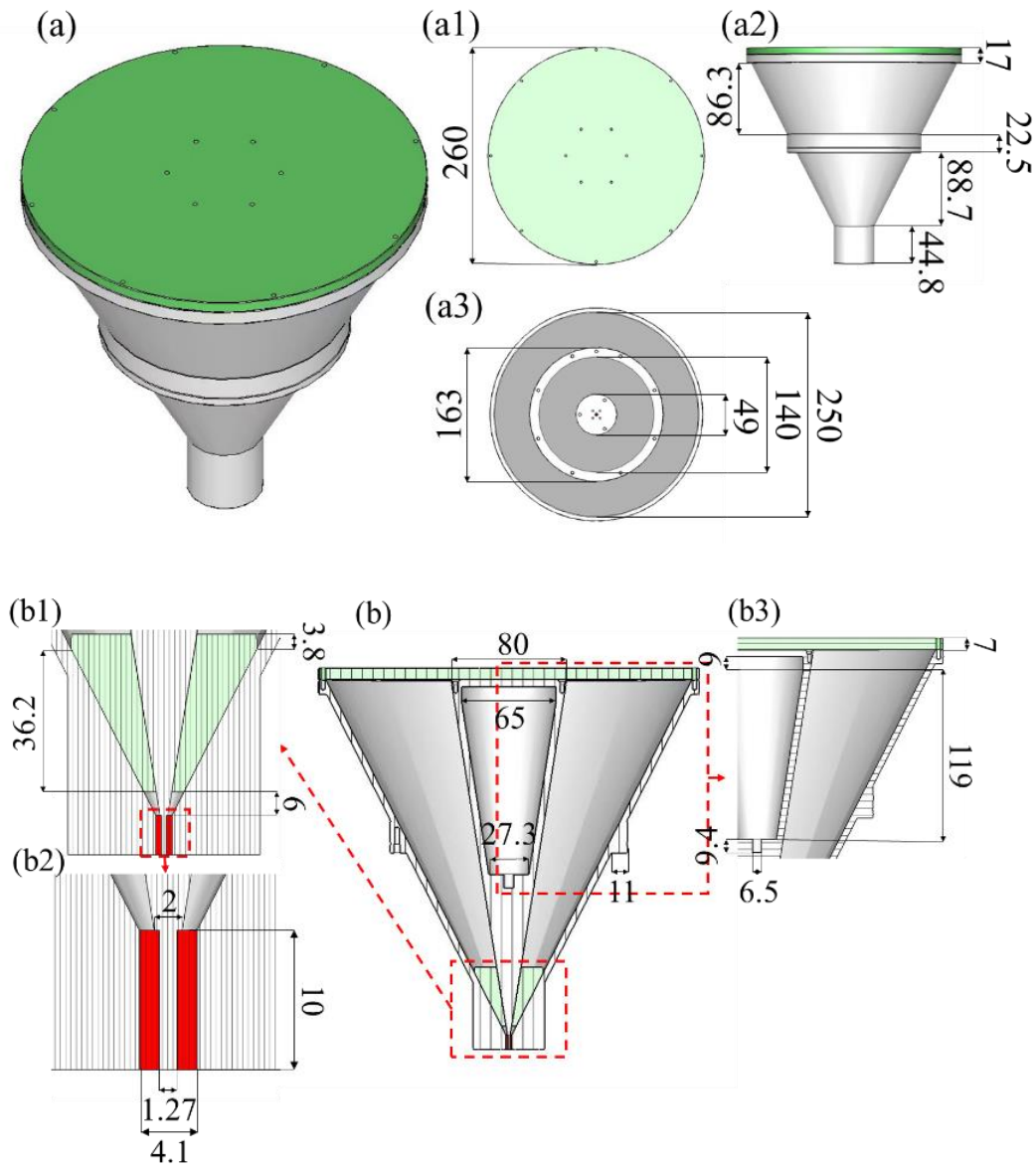


Fig. S1. Structural parameters of the broadband conical coaxial horn antenna. Dimensions are in millimeters (mm). (a) The overall antenna structure, where the gray areas represent Perfect Electric Conductor (PEC) material, and the green areas represent the supporting dielectric (relative dielectric constant 1.3): (a1) top view; (a2) side view; (a3) bottom view with circular holes used for securing different sections of the antenna during machining using M3 screws. (b) Longitudinal cross-section of the antenna: (b1~b3) detailed enlargements of specific sections.

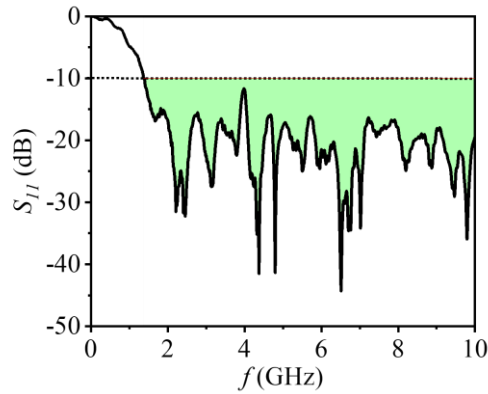


Fig. S2. Measured reflection coefficient for the broadband conical coaxial horn antenna. The measured reflection coefficient remains below -10 dB in the 1.3-10 GHz frequency range, indicating that the designed coaxial horn's operating bandwidth can cover the spectral range below 10 GHz for generating electromagnetic toroidal pulses with parameters $q_1 = 0.01\text{m}$ and $q_2 = 50q_1$.

2. Measurement method for E_r component

We utilized a planar microwave anechoic chamber for measuring the spatial electromagnetic fields of the broadband conical coaxial horn antenna, as shown in Fig. S3. The antenna was moved to the desired measurement area using a scanning frame. The vector network analyzer was connected to the transmitting and receiving antennas, and we measured S_{21} to obtain the magnitude and phase characteristics of the electromagnetic field at different spatial positions.

The receiving antenna used in the experiment was the broadband conical coaxial horn antenna we designed, while the transmitting antenna was a standard rectangular horn antenna with a frequency range of 1-18 GHz. Due to the rotational symmetry of the broadband conical coaxial horn antenna's structure, we only needed to measure the electric field within a rectangular region on one side along the central axis of the horn antenna. Rotating this rectangular region around the central axis by 360° provided the electric field distribution in three-dimensional space.

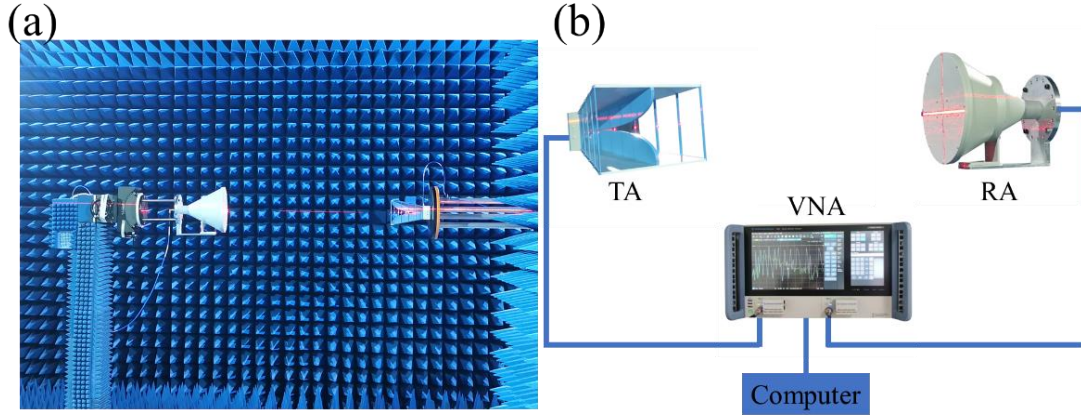


Fig. S3. Spatial magnitude and phase measurement setup for the broadband conical coaxial horn antenna. (a) Overview of the anechoic chamber environment. (b) Setup of the measurement system. In the diagram, VNA, TA, and RA correspond to a vector network analyzer, transmitting antenna, and receiving antenna, respectively. The transmitting and receiving antennas are standard antennas and the broadband conical coaxial horn antenna under measurement, respectively.

The polarization direction of the transmitting standard horn antenna was adjusted to align with the radial direction of the broadband conical coaxial horn antenna to measure the E_r component. The scanning system was programmatically controlled to scan within the desired plane, allowing us to obtain the field distribution in the target plane.

3. Method for calculating the time-domain field from the measured spectral distribution

The simulated time-domain results were obtained using the time-domain simulator in COMSOL, directly exciting the broadband conical coaxial horn antenna with the signal $g_f(t) = \int_{-\infty}^t E_r(\tau, r = r_f, z = 0) d\tau$ based on the canonical Hellwarth-Nouchi toroidal pulse' E_r component at the radius $r = r_f$ with the widest spectral range on the $z=0$ m plane.

On the other hand, the experimental time-domain results were acquired through spectral measurements. We obtained the spatial magnitude characteristic (Fig. 3) and spatial phase characteristics (Fig. S4) of the broadband conical coaxial horn antenna using the aforementioned frequency domain measurement method and computed the time-domain field through inverse Fourier transformation. These results were instrumental in demonstrating the actual generation of electromagnetic toroidal pulses. Our experimental measurement covered field distributions in the frequency range of 0.05-10 GHz with a frequency increment of 0.05 GHz.

The amplitude-frequency response $E_{rabs}(f, r, z)$ and phase-frequency response $E_{rarg}(f, r, z)$ are measured after system calibration, then the spatiotemporal response T_{meas} of the designed broadband conical coaxial horn antenna can be derived using the Fourier transformation process:

$$F_{meas}(f, r, z) = E_{rabs}(f, r, z) * e^{i*E_{rarg}(f, r, z)} \quad (s1)$$

$$T_{meas}(t, r, z) = \frac{1}{2\pi} \int_{-\infty}^{+\infty} F_{meas}(\omega, r, z) e^{i\omega t} d\omega \quad (s2)$$

Given that an antenna can be considered as a time-domain differentiator, we fed the broadband conical coaxial horn antenna with the time-domain integration signal $g_f(t)$. This results in the spatiotemporal field distribution $E_{st}(t, r, z)$ generated by the broadband conical coaxial horn antenna:

$$E_{st}(t, r, z) = T_{test}(t, r, z) \otimes g_f(t) \quad (s3)$$

where \otimes denotes convolution. The spatiotemporal field distribution calculated using the measured amplitude-frequency response and phase-frequency response is presented in Fig. 2.

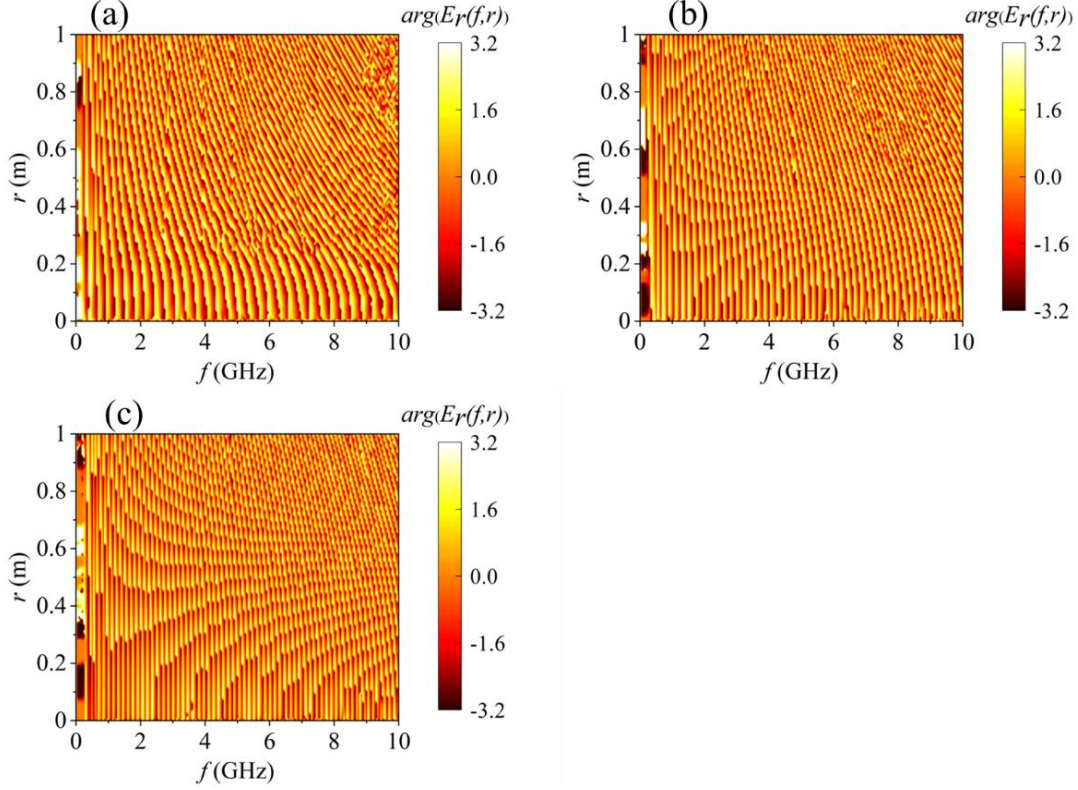


Fig. S4. Measured spatial phase characteristics at different positions of the broadband conical coaxial horn antenna. (a), (b), and (c) respectively show the spatial phase characteristics of the E_r component when the spacing between the transmitting and receiving antenna apertures was 5 cm, 50 cm, and 100 cm.

4. Method for calculating E_z component using measured E_r component

Due to the strict rotational symmetry of the designed broadband conical coaxial horn antenna, the electromagnetic pulses it generates consist solely of E_r and E_z components. The E_z component can be determined from the measured E_r component using a transformation formula based on Gauss's law [13], as follows:

$$E_z(r, z) = - \int_{\alpha}^z \frac{\partial E_r(r, z')}{\partial r} dz' \quad (s4)$$

where α is selected as a reference point where the field is zero. The E_z component obtained from measured E_r according Eq. (s4) is referred to as the experimental results, and its comparison with the E_z components generated by directly exciting the broadband conical coaxial horn antenna with $E_s(t, r, z)$ in simulations and the E_z component of canonical Hellwarth-Nouchi toroidal pulse is depicted in Fig. S5. The measurement, simulation results, and canonical Hellwarth-Nouchi toroidal pulse exhibit similar trends.

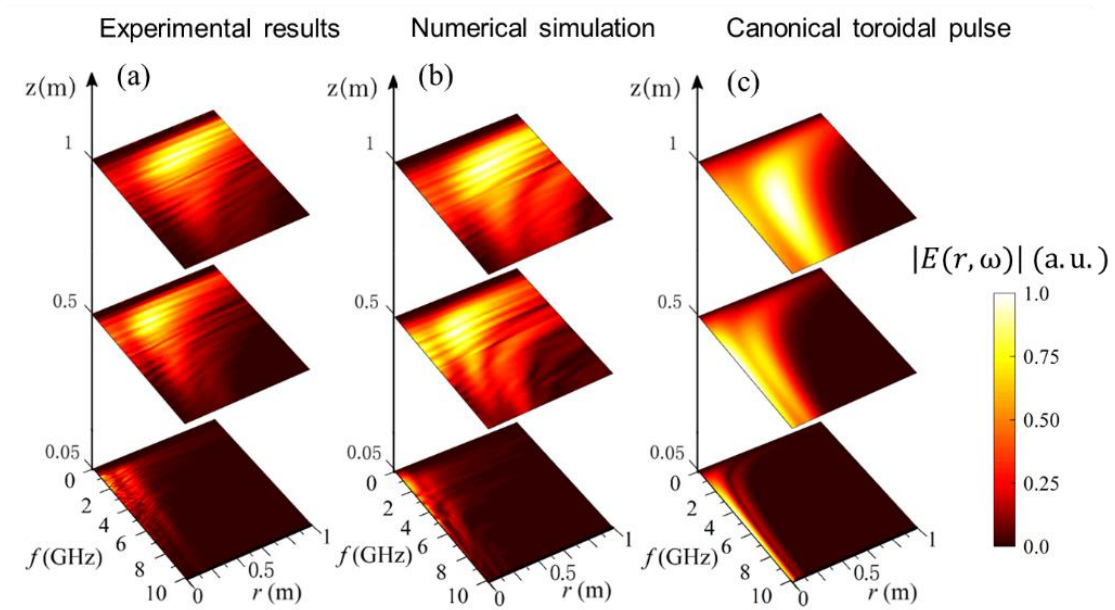


Fig. S5. Spatiospectral maps of E_z component. The maps respectively correspond to the E_z components generated by the broadband conical coaxial horn antenna at distances of 5cm, 50cm, and 100cm from the aperture, in contrast to the canonical Hellwarth-Nouchi toroidal pulse.

Similar to the E_r component, using Eq. (s3), we can compute the spatiotemporal field distribution corresponding to the measured E_z component. The spatiotemporal field distribution of the E_z component generated by the broadband conical coaxial horn antenna as it propagates to $z=5\text{cm}$, 50cm , and 100cm is compared to that of canonical Hellwarth-Nouchi toroidal pulse, as shown in Fig. S6. The combination of E_z and E_r components in the spatiotemporal field distribution

allows for the construction of the spatiotemporal vector field distribution, where skyrmionic textures can be observed, as depicted in Fig. 5.

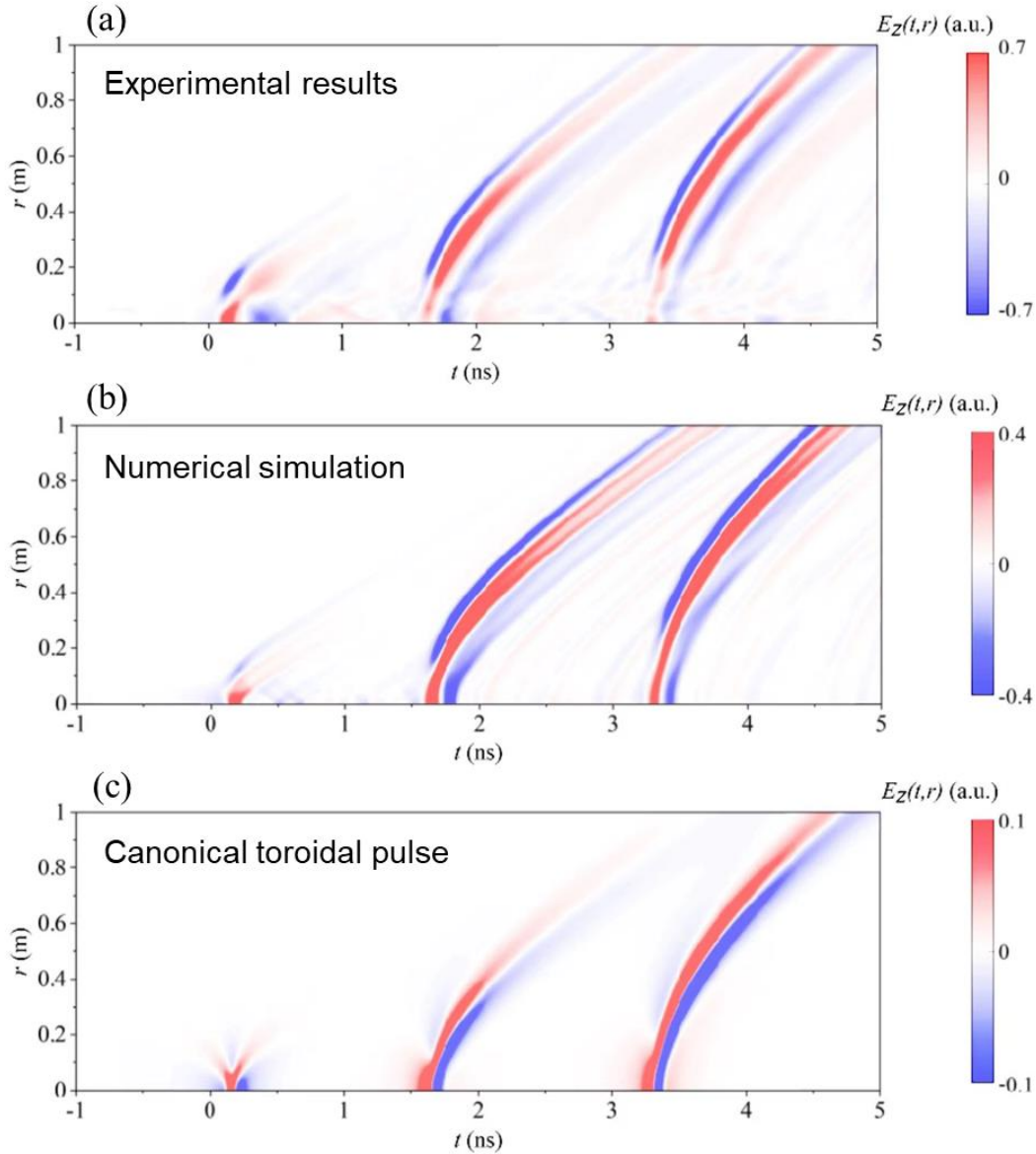


Fig. S6. Normalized spatiotemporal fields of the E_z component at distances of 5cm, 50cm, and 100cm from the antenna's aperture. (a) Measured and transformed through inverse Fourier transformation. (b) Obtained through COMSOL time-domain simulations. (c) Canonical Hellwarth-Nouchi toroidal pulse.

5. Method for spatiotemporal nonseparability calculation

To quantify the spatiotemporal nonseparability of the pulses generated by the broadband conical coaxial horn antenna and its evolution after radiation, this study employed the method proposed in [16] to calculate the changes in concurrence (con) and entanglement of formation (EoF) for the radiated pulses at the antenna aperture. In the computation of con and EoF, two distinct states were introduced:

(1) The spectral state is used to describe monochromatic electromagnetic waves. The spectral state corresponds to the radial position $r_{\lambda_i}(z)$ where the energy density of the electromagnetic field is maximal at any longitudinal location, defined as $r_{\lambda_i}(z) = \max_r(I_{\lambda_i}(r, z))$. The function $\varepsilon_{\lambda_i}(r, z)$ is introduced to describe the distribution of energy density of the monochromatic electromagnetic field in the radial direction:

$$\varepsilon_{\lambda_i}(r, z) = \begin{cases} \sqrt{I_{\lambda_i}(r, z)} & r_{\lambda_i}(z) - \Delta_{\lambda_i}(z)/2 < r < r_{\lambda_i}(z) + \Delta_{\lambda_i}(z)/2 \\ 0 & \text{otherwise} \end{cases} \quad (\text{s5})$$

where $\Delta_{\lambda_i}(z) = \min_j |r_{\lambda_i}(z) - r_{\lambda_j}(z)|$ ($i, j = 1, 2, \dots, n$ and $i \neq j$).

(2) Spatial states are used to describe electromagnetic waves at a specific location in space. This location is defined with a radial ratio $\eta_i(z) = r(z) / r_{\max}(z)$, where is the position in the radial position $r_{\max}(z)$ where the total energy density of the electromagnetic field is maximal, denoted as $r_{\max}(z) = \max_r(I(r, z))$. Similarly, the function $\varepsilon_{\eta_i}(r, z)$ is introduced to describe the distribution of total energy density $I_{\lambda}(r, z)$ of the electromagnetic field in the radial direction:

$$\varepsilon_{\eta_i}(r, z) = \begin{cases} \sqrt{I_\lambda(r, z)} & \eta_i(z) * r_{\max}(z) - \Delta_{\eta_i}(z) / 2 < r < \eta_i(z) * r_{\max}(z) + \Delta_{\eta_i}(z) / 2 \\ 0 & \text{otherwise} \end{cases} \quad (\text{s6})$$

where $\Delta_{\eta_i}(z) = \min_j |\eta_i(z) * r_{\max}(z) - \eta_j(z) * r_{\max}(z)|$ ($i, j = 1, 2, \dots, n$ and $i \neq j$).

The tomography matrix is defined as $M(z) = \{c_{i,j}(z)\}$, $c_{i,j}(z) = \int \varepsilon_{\eta_i}(r, z) \varepsilon_{\lambda_j}(r, z + \Delta z) * dr$:

$$M = \begin{pmatrix} c_{1,1} & c_{1,2} & \dots & c_{1,n} \\ c_{2,1} & c_{2,2} & \dots & c_{2,n} \\ \vdots & \vdots & \ddots & \vdots \\ c_{n,1} & c_{n,2} & \dots & c_{n,n} \end{pmatrix} = \begin{pmatrix} m_1 \\ m_2 \\ \vdots \\ m_n \end{pmatrix}. \quad (\text{s7})$$

Noted $v(z) = (m_1, m_2, \dots, m_n)^T$, the state density matrices are $M_{\text{density}}(z) = v(z)v^T(z)$, then we can the two parameters, concurrence (con) and entanglement of formation (EoF), measuring the strength of spatiotemporal non-separability:

$$\text{Con}(z) = \frac{\sqrt{2[1 - \text{Tr}(\rho_A^2(z))]}{\sqrt{2(1 - 1/n)}}, \quad (\text{s8})$$

$$\text{EoF}(z) = \frac{-\text{Tr}[\rho_A(z) \log_2(\rho_A(z))]}{\log_2(n)}. \quad (\text{s9})$$

where ρ_A is the reduced matrix [16].

Additionally, we calculated the similarity between the generated electromagnetic toroidal pulses and canonical Hellwarth-Nouchi toroidal pulse using the fidelity F :

$$F = \text{Tr}(M_{\text{density}}^{\text{gen}}(z) * M_{\text{density}}^{\text{ideal}}(z)) \quad (\text{s10})$$

where $M_{density}^{gen}(z)$ and $M_{density}^{ideal}(z)$ are the density matrices for the generated and canonical Hellwarth-Nouchi toroidal pulse, respectively.

Similar to the measured state-tomography matrix $\{c_{i,j}\}$, with element $c_{i,j} = \int \varepsilon_{\eta_i} \varepsilon_{\lambda_j}^* dr$ representing the overlap of spatial and spectral states, the simulated one also indicates a poor match to the canonical Hellwarth-Nouchi pulse at proximity to the antenna and it gradually diagonalizes upon propagation, as shown in Fig. S7, where ε_{λ_j} and ε_{η_i} describe the distributions of monochromatic energy density and total energy density [16]. The fidelity exceeds 0.7, indicating a high resemblance to the canonical Hellwarth-Nouchi toroidal pulse. The state-tomography matrix initially exhibits a disordered state in close proximity to the antenna and gradually diagonalizes after propagating a certain distance. Similarly, the simulated and measured state density matrices near the broadband conical coaxial horn antenna exhibit a disordered state and becomes more uniform as the propagation continues (Fig. S8).

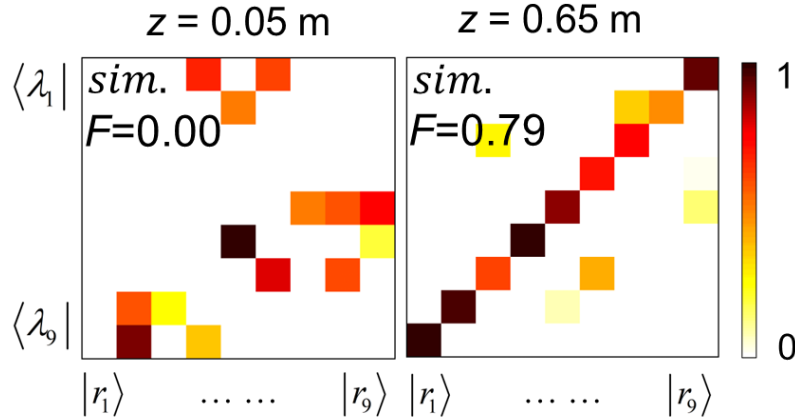


Fig. S7. Simulated state-tomography matrix. The fidelity exceeds 0.7 at $z = 0.65\text{m}$, indicating a high resemblance to the canonical Hellwarth-Nouchi toroidal pulse. The state-tomography matrix initially exhibits a disordered state in close proximity to the antenna and gradually diagonalizes after propagating a certain distance.

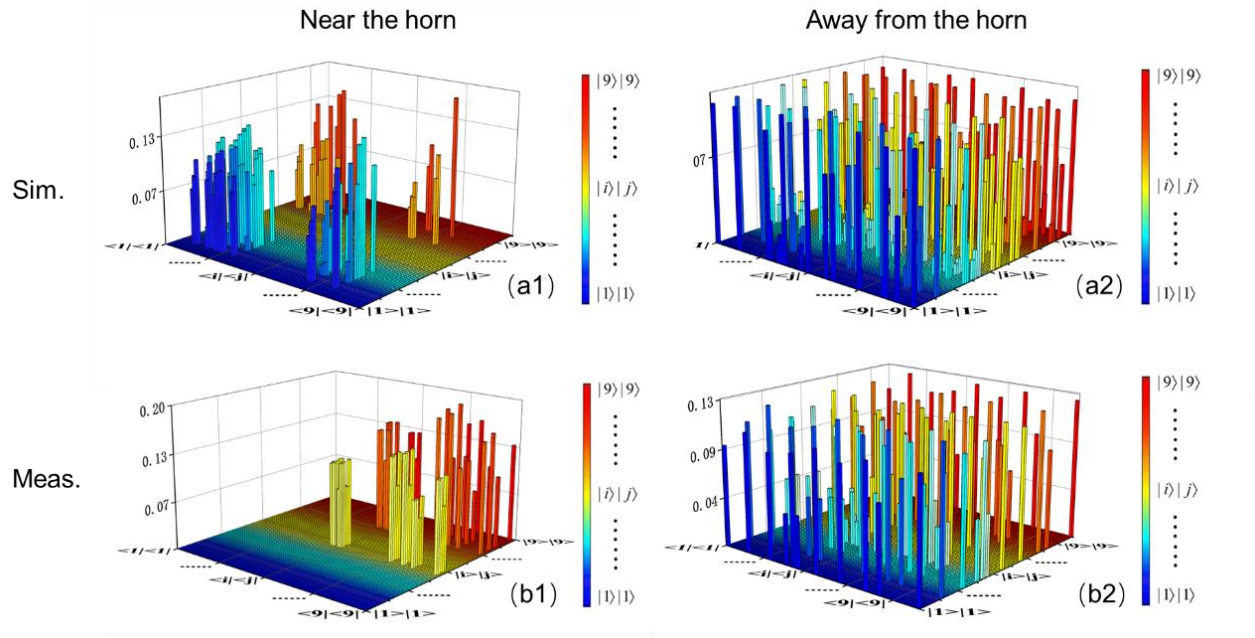


Fig. S8. (a) Simulated and (b) measured state density matrices. (a1) and (b1), at a location near the broadband conical coaxial horn antenna ($z=0.05\text{m}$); (a2) and (b2) after propagating a certain distance ($z=0.65\text{m}$).

The spatiotemporal nonseparability is also visually evident in the propagation trajectories of individual components of the spatiotemporal pulses. Unlike traditional broadband beam profiles such as encountered vector-polarized Laguerre-Gauss (LG) beams, electromagnetic toroidal pulses do not exhibit spectral component crossing during propagation [16]. The trajectories of different frequency components during the propagation of simulated, measured, and canonical Hellwarth-Nouchi toroidal pulse are shown in Fig. S9. It can be observed in the figure that, near the immediate vicinity of the broadband conical coaxial horn antenna (near $z=0$), the different frequency components from both simulation and measurement exhibit spectral crossings during propagation. However, as they continue to propagate, the trajectories of various frequency components generated by the broadband conical coaxial horn antenna no longer intersect, demonstrating

isodiffracting characteristics. This aligns with the trend of Con and EoF gradually approaching unity (Fig. 4).

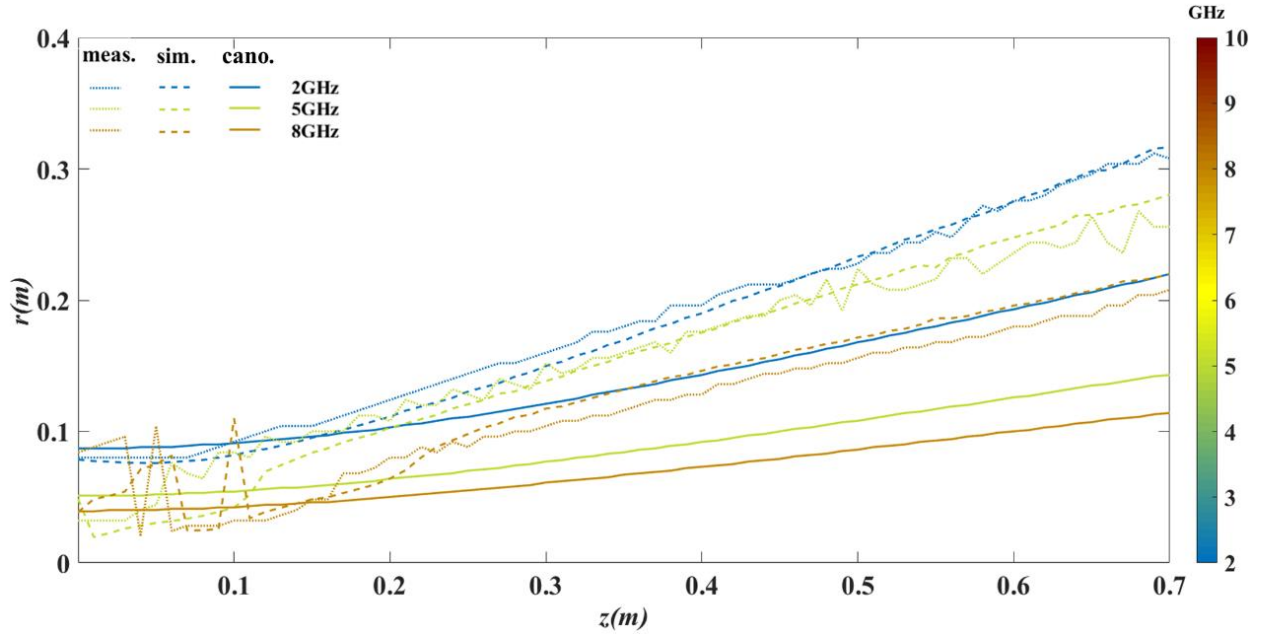


Fig. S9. The trajectories of different frequency components during the propagation of simulated, measured, and canonical Hellwarth-Nouchi toroidal pulse. Near the immediate vicinity of the broadband conical coaxial horn antenna (near $z=0$), the different frequency components from both simulation and measurement exhibit spectral crossings during propagation. The trajectories of various frequency components generated by the broadband conical coaxial horn antenna no longer intersect as propagation, demonstrating isodiffracting characteristics.

Due to the relatively small aperture and narrower band of the horn antenna, the spectral trajectories in both simulation and measurement diverge faster compared to canonical Hellwarth-Nouchi toroidal pulse. However, their divergence rates are consistent with those of truncated electromagnetic toroidal pulses due to aperture limitations.

6. Space-time nonseparability of aperture truncated toroidal electromagnetic pulses

In comparison to the field distribution of canonical Hellwarth-Nouchi toroidal pulse at the $z=0$ position, the field distribution at the aperture of the broadband conical coaxial horn antenna exhibits two distinct characteristics: a smaller aperture area and a single time-domain signal excitation. To visually demonstrate the characteristics of electromagnetic toroidal pulses under non-canonical conditions due to aperture truncation and non-canonical initial field distributions, we conducted simulation calculations of the propagation of non-canonical Hellwarth-Nouchi toroidal pulse under various scenarios using COMSOL's electromagnetic transient solver. Assuming the electric field distribution of canonical Hellwarth-Nouchi toroidal pulse at the $z=0$ plane is represented as $E_{\text{ideal}}(r, t)$, we set up aperture truncated source (s11), aperture truncated single location source (s12), and aperture truncated random source (s13):

$$E(r, t) = \begin{cases} E_{\text{ideal}}(r, t) & r < r_0 \\ 0 & r > r_0 \end{cases}, \quad (\text{s11})$$

$$E(r, t) = \begin{cases} E_{\text{ideal}}(r=r_1, t) & r < r_0 \\ 0 & r > r_0 \end{cases}, \quad (\text{s12})$$

$$E(r, t) = \begin{cases} E_{\text{ideal}}(r=r_{\text{random}}, t) & r < r_0 \\ 0 & r > r_0 \end{cases}, \quad (\text{s13})$$

where r_0 , r_1 , and r_{random} represent the truncation radius, a specific radius, and a random radius, respectively. When taking $r_0=5q_1$, $r_1=2.5q_1$, and $r_{\text{random}} < r_0$, the corresponding sources in Equations (s11~s13) have frequency domain and time domain distributions as shown in Fig. S10.

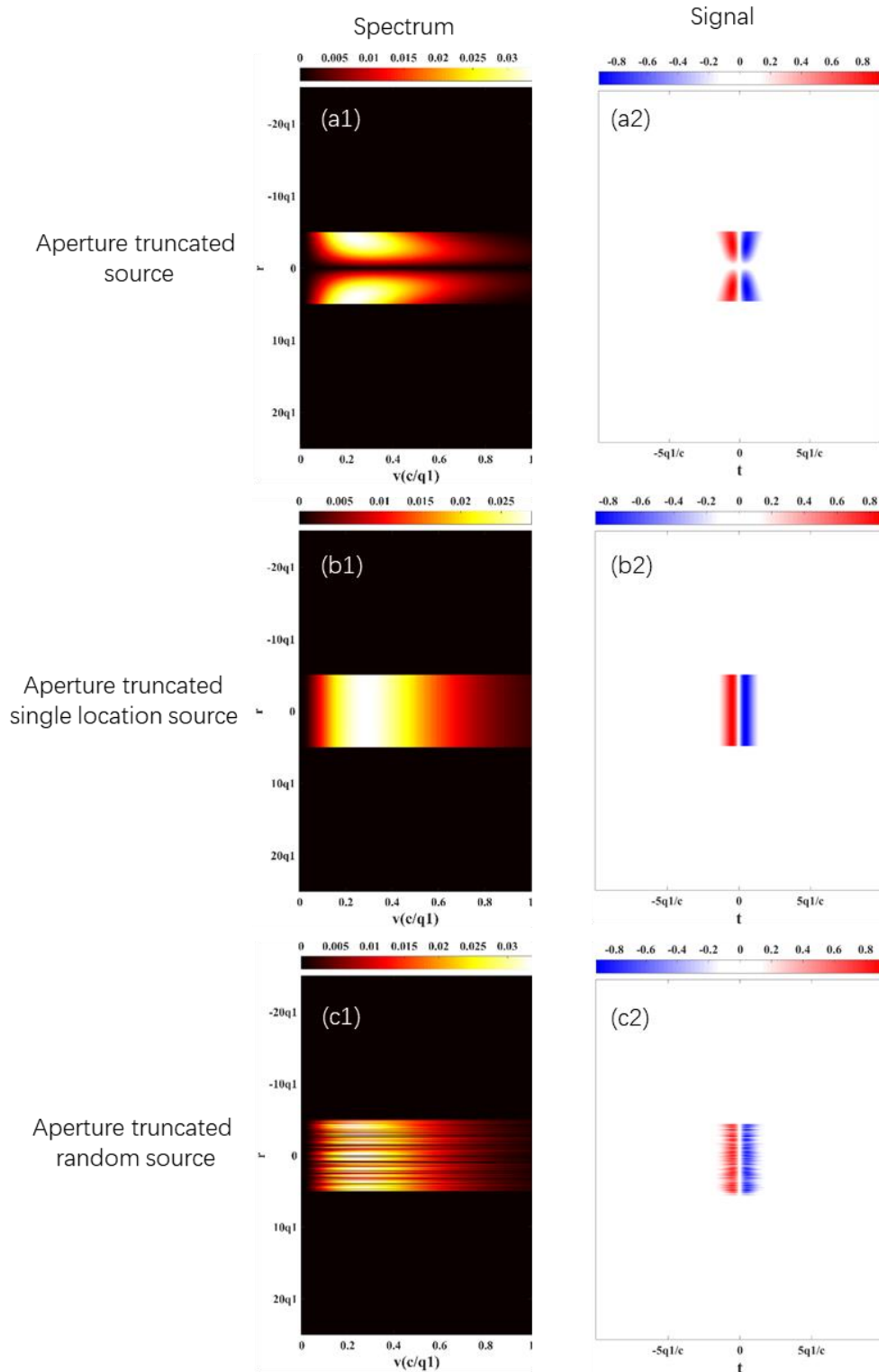


Fig. S10. (a) Aperture truncated source, (b) aperture truncated single location source, and (c) aperture truncated random source. (a1~c1) and (a2~c2) correspond frequency spectrum and time-domain signal, respectively.

Calculations were conducted for the electromagnetic toroidal pulses' spatiotemporal nonseparability under various levels of aperture truncation in the case of the aperture truncation source, as shown in Fig. S11(a). The results indicate that the spatiotemporal nonseparability of electromagnetic toroidal pulses evolve towards higher space-time nonseparability and closer proximity to the canonical during propagation under different degrees of aperture truncation, even when the remaining energy after truncation is only 1.9% of the original electromagnetic toroidal pulses. Similarly, whether replacing the field at a single radius with that at all radius positions or swapping the field at different radius positions, electromagnetic toroidal pulses can regain their spatiotemporal non-separability after propagating a certain distance, where concurrence (con) and entanglement of formation (EoF) increase to around 1 (Figs. S11(b) and (c)). Therefore, the broadband conical coaxial horn antennas capable of emitting ultra-wideband radially polarized electromagnetic waves can be used to generate electromagnetic toroidal pulses even though the field distribution is not exactly the same as that of canonical Hellwarth-Nouchi toroidal pulse at the $z=0$ position.

7. Spatiotemporal vector field distribution

The combination of E_z and E_r components in the spatiotemporal field distribution allows for the construction of the spatiotemporal vector field distribution, where skyrmionic textures can be observed, as depicted in Fig. 5. Fig. 5 displays the electric field vectors on longitudinal cross-sections at different time instances. Due to the rotational symmetry of the structure, the electric field data for the entire space can be obtained by applying rotational symmetry to the longitudinal cross-section data.

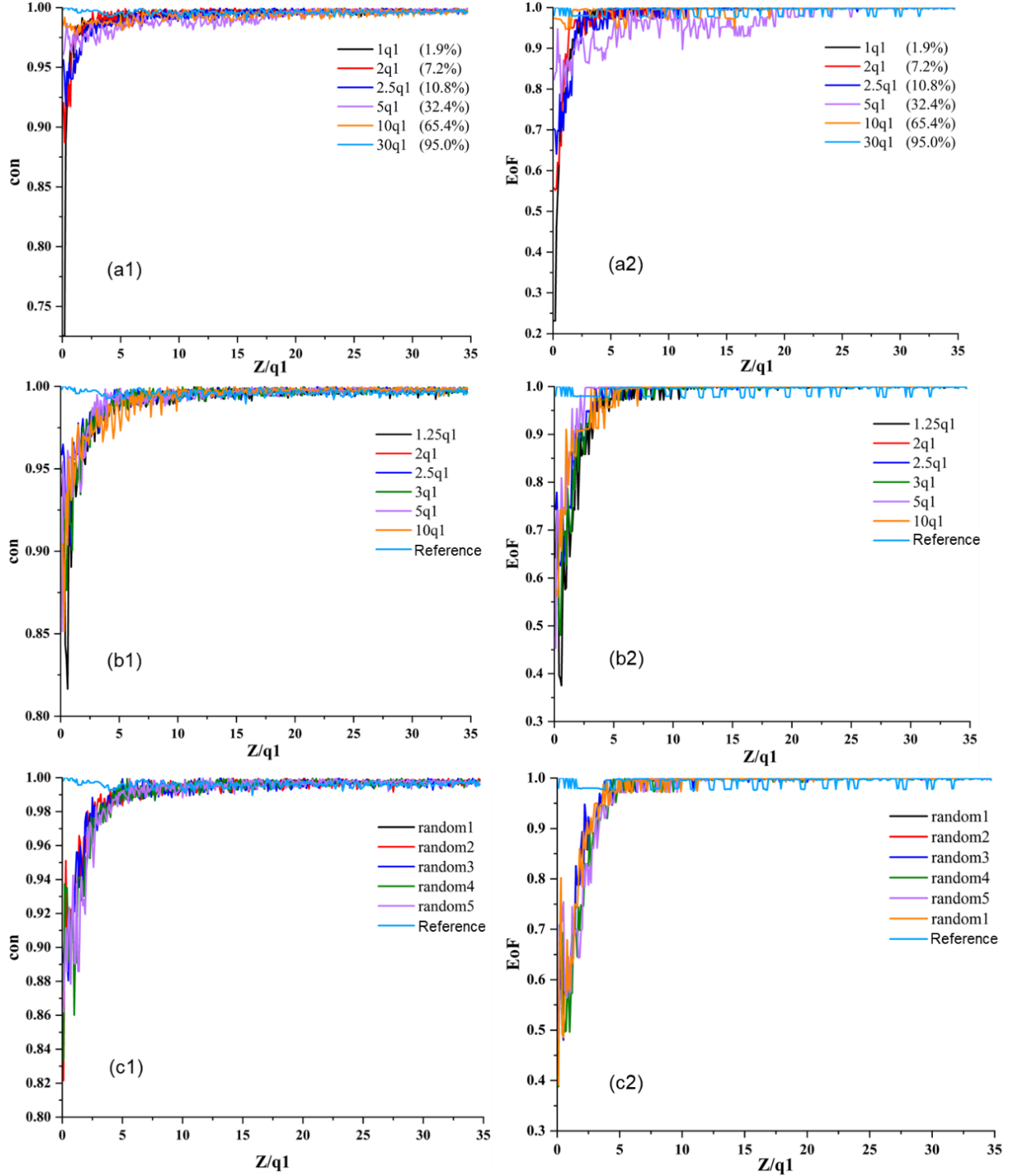


Fig. S11. Concurrence (con) and entanglement of formation (EoF) during propagation. The fields are emitted by: (a) aperture truncated source, (b) aperture truncated single location source, and (c) aperture truncated random source. In (a1) and (a2), each curve corresponds to the value of

the retained aperture radius after truncation, with the percentage value in parentheses denoting the ratio of the remaining energy after aperture truncation to the energy of perfect electromagnetic toroidal pulses. (b1) ~ (c2) have a common aperture radius $r_0=30q_1$, and the reference curve represents the situation where the original electromagnetic toroidal pulses' field distribution is maintained within the truncated aperture, corresponding to the case in (a1) and (a2) with $r_0=30q_1$. In (b1) and (b2), each curve corresponds to the position used to replace the field within the radius range $r < r_0$. (c1) and (c2) feature curves corresponding to different random source field distributions.

The simulated spatiotemporal vector field distributions and those of canonical Hellwarth-Nouchi toroidal pulses are shown in Fig. 12S. Similar to the measured results in Fig. 5 in the manuscript, the electric field has both radial component E_r and longitudinal component E_z . The field features vector singularities, including saddle points on central axis and vortex rings away from the central axis.

The topological properties of the two-dimensional skyrmion model can be characterized by the skyrmion number, which is a topological invariant. The skyrmion number is the spatial integral of the topological charge density and can be calculated using the following formula [30]:

$$N_s(\mathbf{r}) = \frac{1}{4\pi} \iint \mathbf{m}(\mathbf{r}) \cdot \left[\frac{\partial \mathbf{m}(\mathbf{r})}{\partial x} \times \frac{\partial \mathbf{m}(\mathbf{r})}{\partial y} \right] dx dy \quad (\text{S14})$$

where $\mathbf{m}(\mathbf{r}) = \frac{\mathbf{E}(\mathbf{r})}{|\mathbf{E}(\mathbf{r})|}$ represents the unit vector used to construct Skyrmions, and $\mathbf{E}(\mathbf{r})$

corresponds to the electric field vector at position $\mathbf{r} = (x, y)$. The size of the calculation space can be determined based on the dimensions of the skyrmions. The boundary for calculating the

skyrmion number is chosen to be the location where the longitudinal electric field appears for the second time. Using Eq. (S14), the skyrmion number is computed, and the results are as depicted in Fig. 5 and Fig. 13S. The obtained value is approximately ± 1 , satisfying the requirement of an almost integer skyrmion number, which indicates the presence of skyrmionic textures in the generated electromagnetic toroidal pulses.

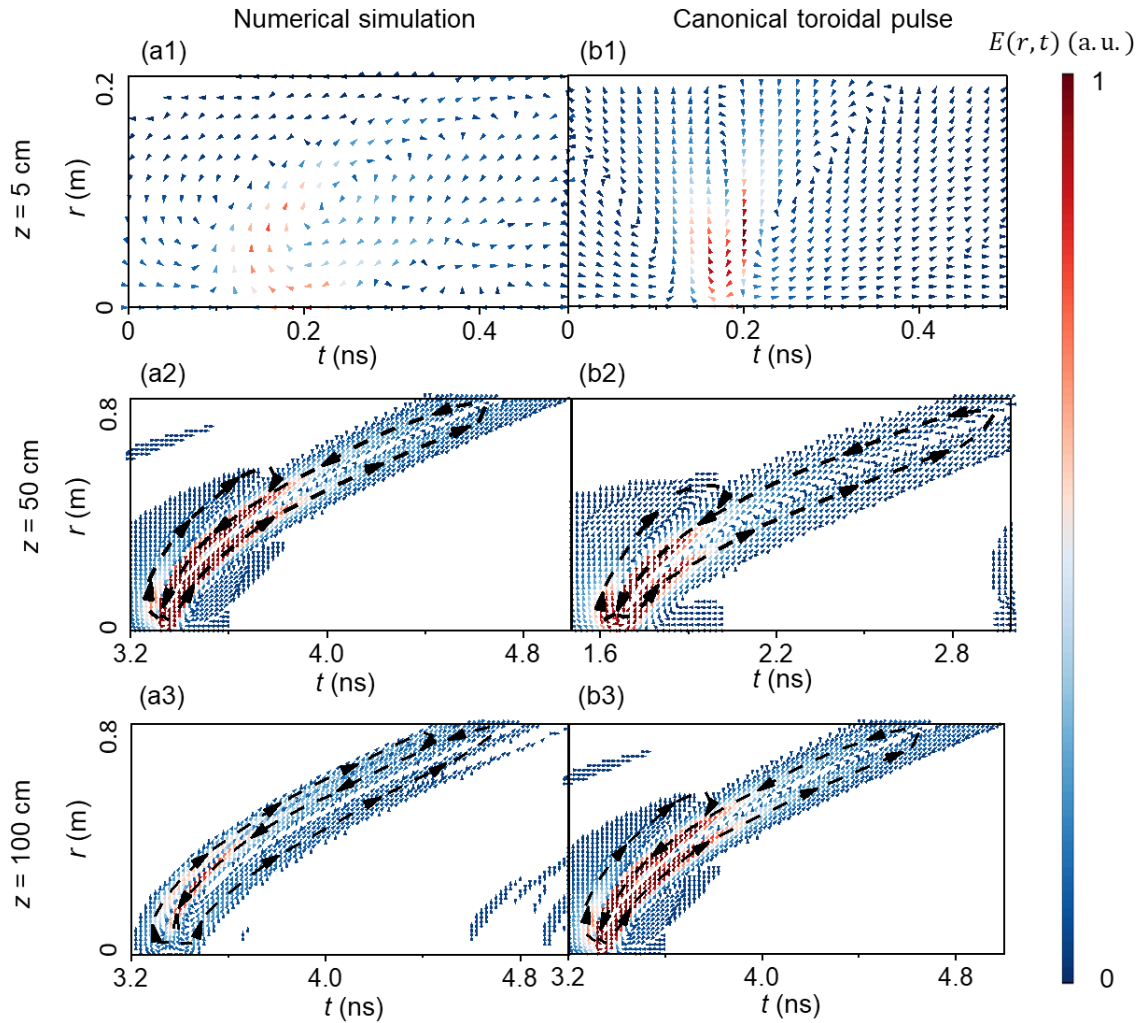


Fig. 12S. Spatiotemporal distribution of vector fields. (a) Numerical simulations and (b) canonical Hellwarth-Nouchi toroidal pulses. (a1)/(b1), (a2)/(b2) and (a3)/(b3) correspond to the toroidal pulses propagating to $z = 5$ cm, 50 cm, and 100 cm, respectively.

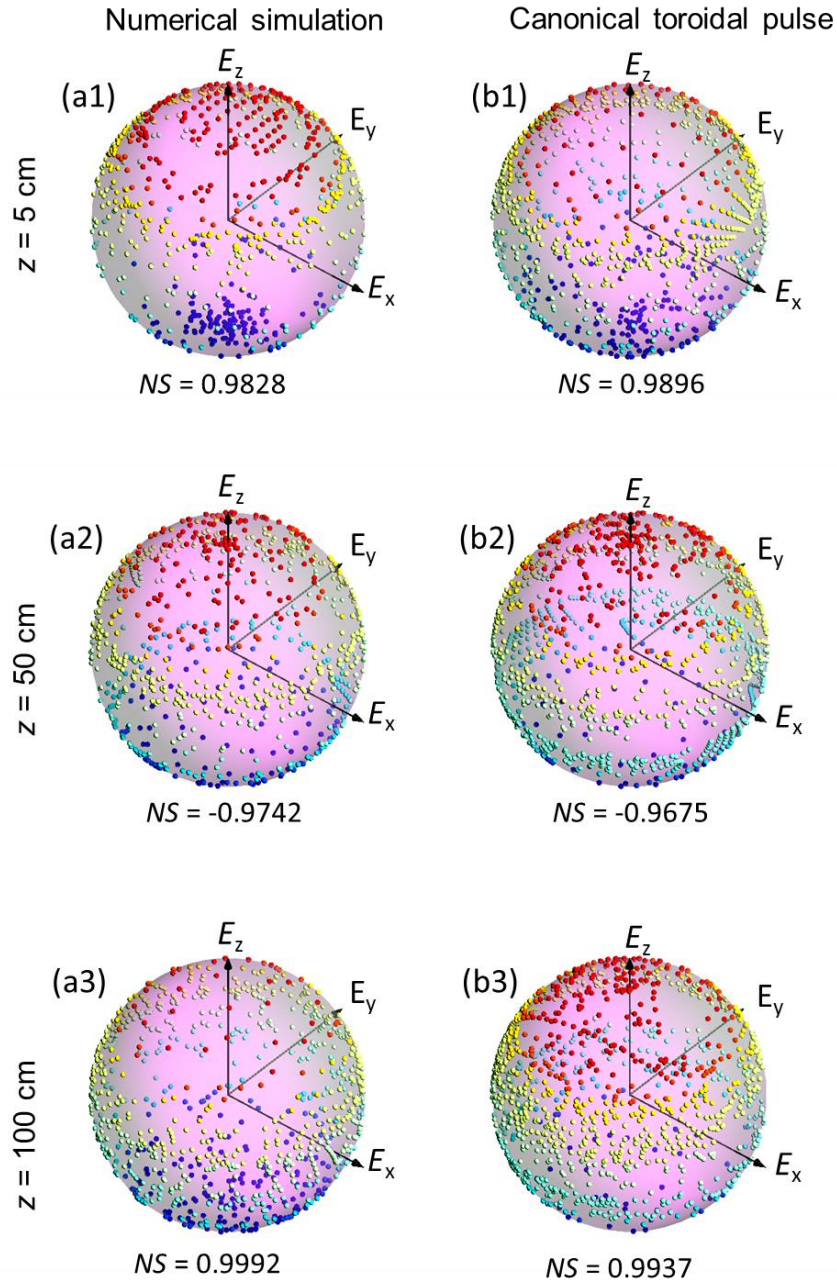


Fig. 13S. The sphere of directions. (a) simulated and (b) canonical Hellwarth-Nouchi toroidal pulse when the pulses propagate to (a1/b1) 5cm, (a2/b2) 50cm and (a3/b3) 100cm from the antenna's aperture. The skyrmion number (NS) in each subfigure is close to 1, representing good skyrmionic textures.

The vector characteristics of skyrmions can also be visually represented through the coverage of the sphere of directions for Cartesian sampling of a skyrmions cell [30]. The sphere of directions refers to the unit sphere with a radius of 1, and the position on the sphere of directions where a vector is mapped depends on the direction in which the vector points. For two-dimensional vectors on the plane $\mathbf{r} = (x, y)$, after normalizing their length and using the origin as the starting point, the location where the vector endpoint represents the mapping of that vector on the sphere of directions. If the coverage of the sphere of directions for the vectors in a two-dimensional target area can completely cover the directional sphere, it can intuitively reflect the existence of skyrmions. The sphere of directions for simulated and canonical Hellwarth-Nouchi toroidal pulse when the pulses propagate to different position are shown in Fig. 13S. The coverage of the sphere of directions fully spans the surface of the sphere, providing a visual confirmation of the presence of skyrmions.

8. Discussion of the coaxial horn's shape

Besides coaxial cone-shaped horn emitter, we also discussed coaxial pentagonal horn, coaxial rectangular horn, and coaxial triangular horn, as shown in Fig. 14S. All the space-time field and spectrum distributions emitted from different coaxial horns are similar to those of the canonical Hellwarth-Nouchi toroidal pulse, although the shapes of coaxial horns are quite different. The coaxial configuration provides the radial polarization and wide emitting bandwidth, which is the key factor for toroidal pulse generation.

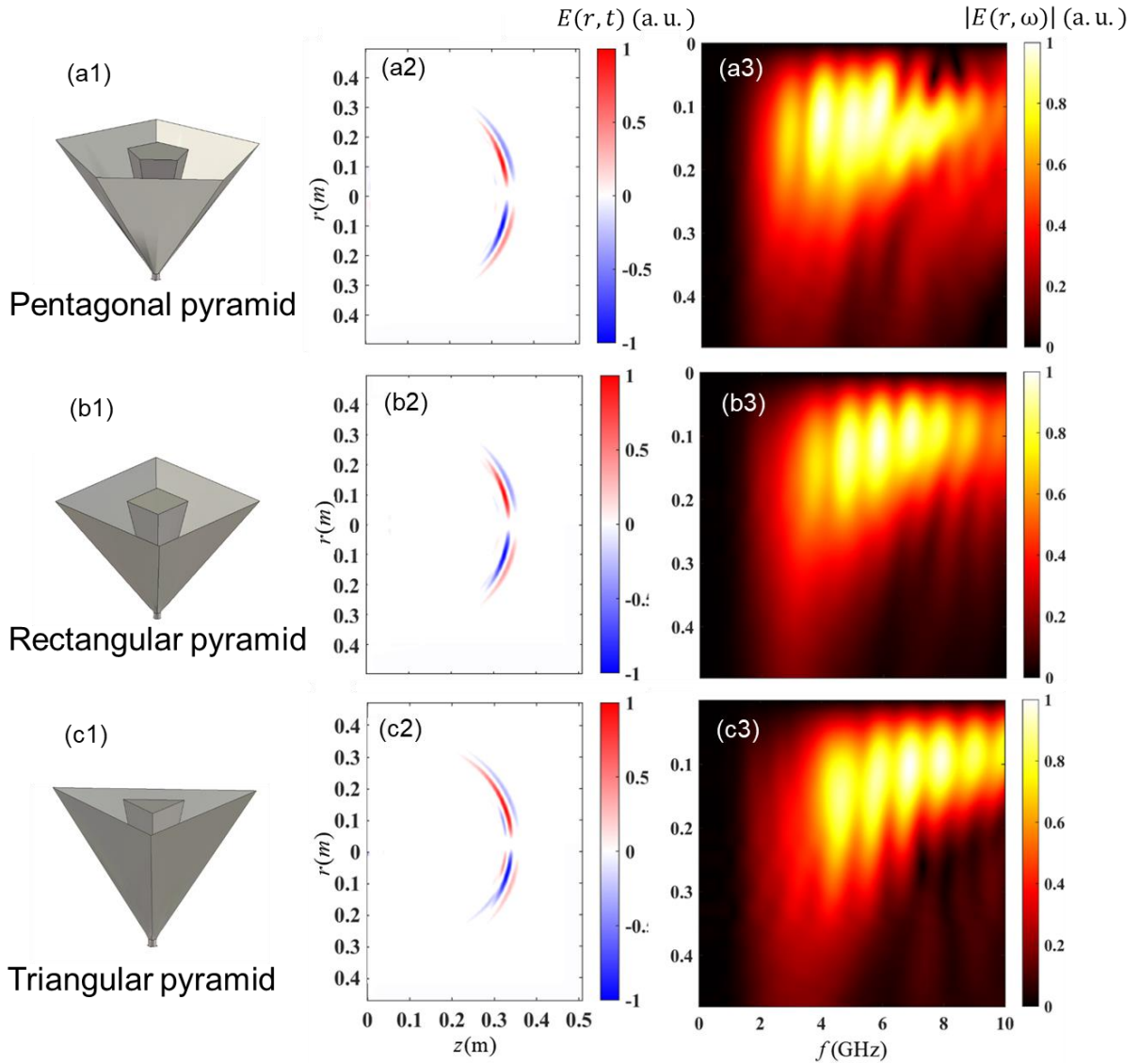


Fig. 14S. Generation of toroidal pulses with different coaxial horn emitters: (a) coaxial pentagonal horn, (b) coaxial rectangular horn and (c) coaxial triangular horn. (a1~c1) Structures of the horn emitters, (a2~c2) space-time field distributions and (a3~c3) spectrum distributions. All the space-time field and spectrum distributions emitted from different coaxial horns are similar to those of the canonical Hellwarth-Nouchi toroidal pulse.